Heteroepitaxial Growth of Colloidal Nanocrystals onto Substrate Films *via* Hot-Injection Routes

Krishna P. Acharya,[†,§] Elena Khon,[†,§] Timothy O'Conner,[†,§] Ian Nemitz,[§] Anna Klinkova,[†,§] Rony S. Khnayzer,[†,‡] Pavel Anzenbacher,[†,‡] and Mikhail Zamkov[†,§,*]

[†]The Center for Photochemical Sciences, [‡]Department of Chemistry, and [§]Department of Physics, Bowling Green State University, Bowling Green, Ohio 43403, United States

ABSTRACT Hot-injection synthesis of colloidal nanocrystals (NCs) in a substrate-bound form is demonstrated. We show that polycrystalline films submerged into hot organic solvents can nucleate the heteroepitaxial growth of semiconductor NCs, for which the ensuing lattice quality and size distribution are on the par with those of isolated colloidal nanoparticles. This strategy is demonstrated by growing lead chalcogenide NCs directly onto solvent-submerged TiO_2 substrates. The resulting PbX/TiO_2 (X = S, Se, Te) nanocomposites exhibit heteroepitaxial interfaces between lead chalcogenide and oxide domains and show an efficient separation of photoinduced charges, deployable for light-harvesting applications. The extendibility of the present method to other material systems was demonstrated through the synthesis of CdS/TiO_2 and Cu_2S/TiO_2 heterostructures, fabricated from PbS/TiO_2 composites *via* cation exchange. The photovoltaic performance of nanocrystal/substrate composites comprising PbS NCs was evaluated by incorporating PbS/TiO_2 films into prototype solar cells.

KEYWORDS: photovoltaics · nanorods · dye-sensitized · Schottky · titanium dioxide

Processing of optoelectronic devices from solutions of colloidal nanocrystals (NCs) is emerging as a powerful alternative to conventional methods of thin film deposition requiring high-vacuum and high-temperature conditions. In addition to bulk material properties, inorganic NCs offer a range of unique characteristics arising from their nanoscale dimensions, which enable continuous tuning of NC energy levels, as well as solution processing of as-prepared nanoparticle colloids into thin film devices. Owing to these advantages, deployment of colloidal NCs for practical applications has been actively explored in the past decade through the development of novel NC-based materials that potentially can reduce the cost and simultaneously improve the performance of several important optoelectronic technologies, including lasers,[1−3] solar cells,[4−22] photocatalysts,[23−26] light-emitting diodes (LEDs),[27−34] biolabels,[35−37] thermoelectric elements,[38,39] field-effect transistors,[40−45] magnetic doping,[46,47] and memory elements.[48−52]

One of the main challenges concerning the development of NC-based device applications is the ability to couple colloidal nanoparticles onto a substrate. Since inorganic NCs are fabricated in solutions, their surfaces retain a layer of organic ligands, which renders the nanoparticle soluble and simultaneously serves as a protective barrier between electrical charges in NCs and their external environment. The presence of such an organic shell prevents an efficient coupling of colloidal NCs to a substrate material, which is a crucial step in the development of many device applications spanning the areas of photovoltaics, photocatalysis, and solid state lighting. For instance, the coupling of NCs onto TiO_2 substrates in NC-sensitized solar cells is often mediated by introducing organic linkers,[17,53−56] which results in an unwanted reduction of the charge transfer rate, and ensuing decline in the device performance. Meanwhile, ligand-free growth of semiconductor NCs *via* SILAR (successive ionic layer adsorption and reaction) or chemical bath deposition (CBD) of the semiconductor material onto TiO_2[18,19,21,57−59] often leads to inferior stability of resulting NCs and wide dispersion of their sizes as compared to organically passivated counterparts.[60]

Here we demonstrate a robust and cost-effective method for coupling semiconductor NCs onto a substrate, which relies on the direct nucleation and growth of organically passivated NCs onto TiO_2 films submerged in organic solvents. Grown directly from the substrate, these nanocrystals represent a novel type of "surface-bound" quantum dots that form heteroepitaxial relationships with the substrate film to enable an efficient interdomain charge transfer at the NC/substrate interface, meanwhile, being fabricated *via* hot-injection routes, these NCs

* Address correspondence to zamkovm@bgsu.edu.

Received for review March 21, 2011 and accepted April 28, 2011.

Published online April 28, 2011
10.1021/nn201064n

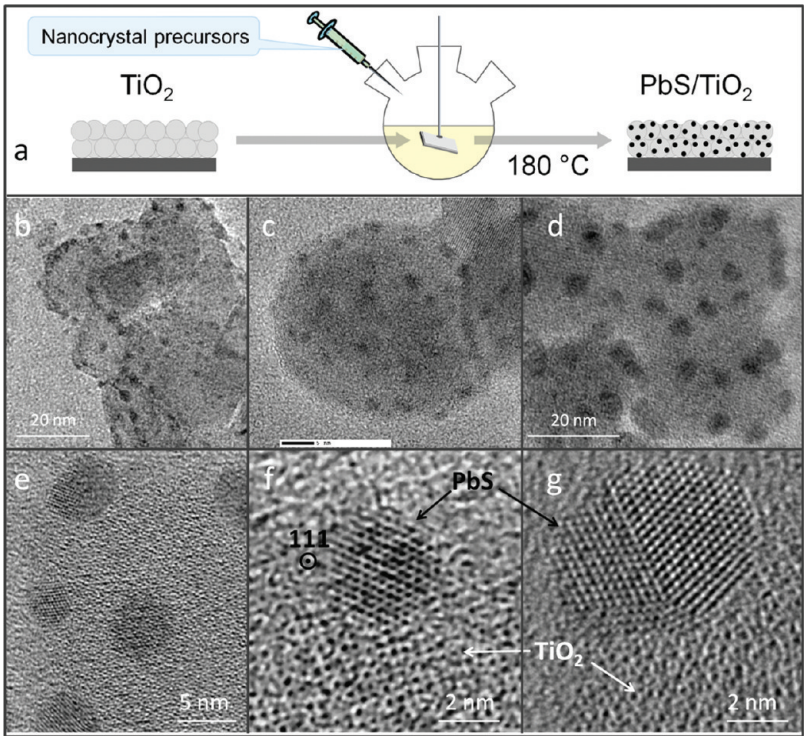

Figure 1. (a) Schematic illustration of the substrate-bound approach to the growth of PbS NCs onto TiO_2 films. (b) Low-magnification TEM image showing a fragment of the PbS/TiO_2 film. (c–g) Fragments of PbS/TiO_2 films comprising small-diameter (c, f) and large-diameter (d, e, g) PbS NCs.

exhibit a narrow distribution of diameters, which is critical for controlling the alignment of energy levels at material boundaries. The photovoltaic performance of fabricated NC/substrate films was demonstrated here by incorporating indium–tin-oxide (ITO)-supported nanocrystal/substrate PbS/TiO_2 composites into solid-type NC-sensitized solar cell architecture.

From the synthetic standpoint, the present method modifies the traditional strategy for growing semiconductor NCs in solutions, to allow a preferential growth of nanocrystals, such as PbX, CdX, and Cu_2X (X = S, Se, Te) onto a polycrystalline substrate, which is placed into the reaction flask prior to the injection of precursors. While in this work, a PbS/TiO_2 nanocrystal–substrate combination was used as a model system along with experimental demonstration of a few other material systems, including PbX/TiO_2 (X = Se, Te), CdS/TiO_2, and Cu_2S/TiO_2, it is anticipated that, based on the similarity of synthetic methods between substrate-bound and isolated colloidal NC/oxide heterostructures, the reported technique could also be extended to other combinations of materials simply by adapting the existing synthetic protocols that were reported previously for the respective colloidal heterostructures.[61–73]

RESULTS AND DISCUSSION

The general strategy for growing colloidal nanocrystals onto a substrate *via* hot-injection routes is based on a two-step procedure, which includes sintering of the film and the subsequent growth of NCs onto a developed substrate *via* injection of organometallic precursors. In this work, a mesoporous oxide film was prepared either from commercial or homemade TiO_2 nanoparticle pastes by sintering its suspension onto an ITO covered glass at 450–500 °C for 1 h. After cooling, the TiO_2 substrate was attached to a metal wire and placed into a three-neck flask containing a degassed mixture of oleylamine and oleic acid. To avoid scratching of the film due to stirring, two identical TiO_2 substrates were coupled together with their blank (glass) surfaces facing outward. This design allowed a free flow of hot reaction solvents near the TiO_2 surface of both substrates without causing any detectable damage to nanoparticle films.

The details of experimental procedures for growing PbX (X = S, Se, Te), CdS, and Cu_2S NCs on the surface of TiO_2 films are provided in the Methods and Supporting Information Sections. Typically, to fabricate PbS/TiO_2 nanocomposite films, a TiO_2 substrate was lowered into a three-neck flask containing 1 mL of oleylamine (OLAM), and 0.5 mL of oleic acid (OA). The mixture was then heated up to 140–180 °C, at which point Pb and S precursors, were simultaneously injected initiating the growth of PbS NCs. After 10–20 min of the growth time, the substrate was pulled out of the solution, and the heating mantle was removed from the flask. To ensure that isolated PbS NCs are completely removed from the sample upon completion of the synthesis, the PbS/TiO_2 film was repeatedly washed with toluene

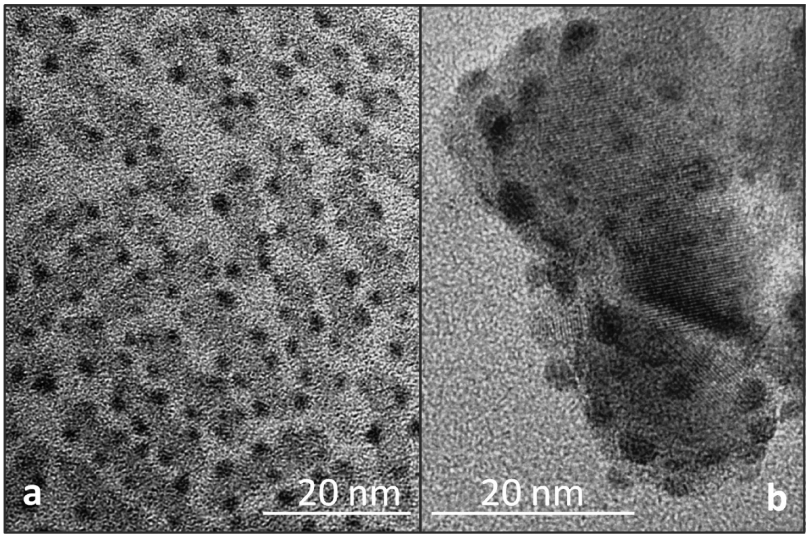

Figure 2. Comparison of the two types of PbS/TiO_2 nanocomposites fabricated in OLAM/OA mixture at 180 °C. (a) PbS NCs grown on the surface of isolated TiO_2 nanorods, (b) PbS domains grown onto the surface of annealed TiO_2 films.

until the changes in its absorption profile became negligible. The absence of isolated nanocrystals was then confirmed using a TEM analysis of random areas sampled from the PbS/TiO_2 film onto a carbon grid.

Typical TEM images of PbS/TiO_2 film fragments in Figure 1 indicate the formation of highly crystalline PbS NCs on the surface of TiO_2 grains. Likewise, growth of PbSe and PbTe NCs on TiO_2 substrates has resulted in the uniform coverage of oxide surface with lead chalcogenide nanoparticles, as shown in Supporting Information Figures SF1 (PbSe) and SF2 (PbTe). Depending on the initial concentrations of injection precursors and the reaction temperature, the average size of PbS NCs could be tuned from 2.5 to 5.0 nm, covering the full range of NC diameters that are expected to produce an efficient photoinduced charge transfer to a TiO_2 acceptor domain (see Figure 5). Depending on the specifics of the synthesis, the size dispersion of substrate-bound PbS domains ranged from 6% to 14% (see Figure 3), which is somewhat broader than the 5−10% range observed for isolated PbS(Se)/TiO_2 heterostructured nanocrystals grown *via* conventional colloidal routes (Figure 2a).[74,75] The crystalline nature of PbS domains was confirmed by the observation of characteristic lattice fringes (Figure 2f,g) that were indexed to known spacing values of the rock-salt cubic (fcc) crystal phase. Judging by the low density of lattice defects observed in investigated specimens, we conclude that the overall crystal quality of PbS "islands" grown on a TiO_2 substrate is comparable to that of PbS NCs grown on suspended TiO_2 nanoparticles in solutions (Figure 2a).

The analysis of TEM images in Figures 1a−d and 2b indicates that both small- and large-diameter PbS NCs appear to be evenly distributed on the surface of oxide grains. Such a growth mechanism has been previously observed for PbS/TiO_2 heterostructures, fabricated *via* chemical bath deposition (CBD),[20] where the formation of islandlike PbS domains was attributed to the minimization of the PbS/TiO_2 interfacial energy associated with the significant strain between PbS and TiO_2 lattices. Unfortunately, the size-dispersion of PbS NCs could not be controlled within the CBD approach due to the lack of synthetic means for modulating the surface tension of growing PbS domains. In the present method, the use of hot-injection approach enables an additional degree of freedom for controlling the shape of composite nanoparticles, associated with the presence of surface-passivating ligands. These molecules modulate the surface tension of growing crystallites, which allows the accomodation of the misfit-induced interfacial strain between the two semiconductor materials and coercion of the narrow distribution of domain sizes. While the smallest dispersion of PbS diameters was achieved when both NC and oxide domains were dressed with surface ligands (5.1%, Figure 2a), the substrate-bound deposition of PbS NCs onto ligand-free TiO_2 films has also proven to facilitate a satisfactory control over NC growth, resulting in a modest 6−14% of the size distribution (Figure 3). Furthermore, as demonstrated in our previous study on solvent-dispersed PbS/TiO_2 heterostructures,[74] the growth of PbS NCs on TiO_2 is expected to occur at locations of lower interfacial stress, which allows for near-epitaxial relationships at the PbS/TiO_2 boundary and the ensuing low-energy expansion of the PbS lattice. These locations are likely to contain irregularities of the TiO_2 lattice that promote a preferential merging of 001 and 100 faces of anatase TiO_2 and rock-salt PbS crystal lattices (Supporting Information, Figure SF3), which otherwise correspond to a substantial 6.9% lattice mismatch.

A ligand-induced approach to controlling the shape of PbS domains was employed through a combination

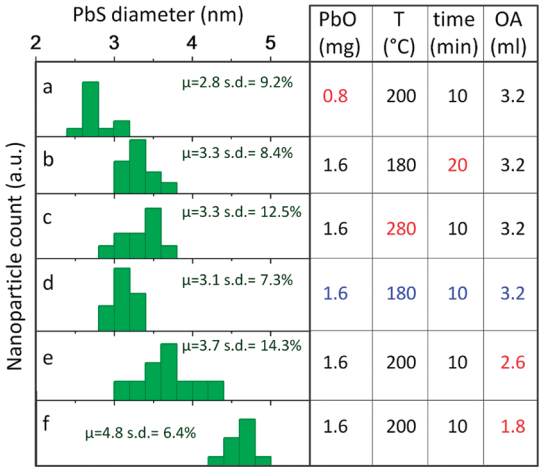

	PbO (mg)	T (°C)	time (min)	OA (ml)
a	0.8	200	10	3.2
b	1.6	180	20	3.2
c	1.6	280	10	3.2
d	1.6	180	10	3.2
e	1.6	200	10	2.6
f	1.6	200	10	1.8

Figure 3. Statistical size distributions of PbS NCs grown onto a TiO_2 film using deferent synthetic conditions. The size distribution obtained with baseline parameters is shown in panel d. The changes relative to the baseline procedure are highlighted in red.

of oleic acid (OA) and oleylamine (OLAM) surfactant molecules. By using a binary mixture of stabilizing ligands, we were able to continuously tune the surface tension of growing nanocrystals, which affects the thermodynamic balance between the surface and interfacial energies of PbS nanoparticles, ultimately changing their shapes. Typically, the formation of large diameter PbS NCs (Figures 1d,g) was favored when the molar ratio of OA (used for the dissolution of Pb precursor) to OLAM was less than 0.6, and the molar ratio of Pb to octadecene (ODE) was 0.4−0.5. On the other hand, if the concentration of OA was high (OA/OLAM ≥ 1), the growth of large-diameter PbS domains was suppressed, and the formation of small, uniformly distributed PbS domains became dominant (Figures 1b,f).

While the ligand concentration plays an important role in determining the overall shape of PbS NCs, the effect of other synthetic variables, such as the reaction temperature and the growth time was found to be less significant. According to the statistical distribution of PbS sizes, reflecting different growth conditions (Figure 3), the change in the solution temperature from 180 (d) to 280 °C (c) produces less than 10% increase in the average NC diameter. Likewise, there is only an 8% enhancement in the size of PbS NCs, when the growth time is increased from 10 to 20 min. Both changes are accompanied by broadening of PbS size distributions, which is consistent with previous studies of isolated PbS NCs showing similar growth kinetics.[76,77] On the basis of the expected correlation between the nanocrystals size and the amount of coprecursors in the reaction mixture, a possibility of controlling the average diameter of PbS NCs by varying the concentration of lead and sulfur precursors in injection solutions was also investigated. It was found that the growth of PbS NCs was completely suppressed at low precursor

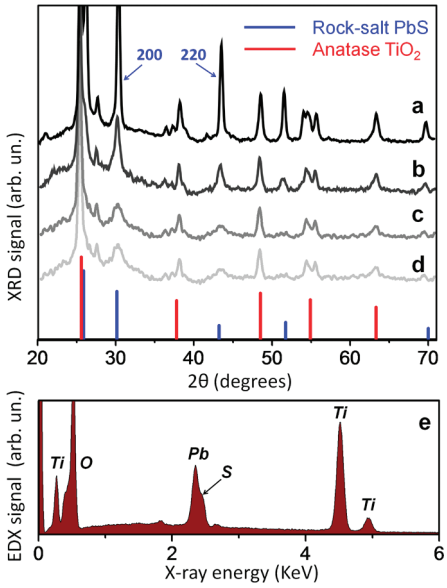

Figure 4. XRD spectra of PbS/TiO_2 films. (a) PbS NCs were grown at 280 °C for 20 min, average diameter, −4.7 nm; (b) PbS NCs were grown at 180 °C for 20 min, average diameter, −4.7 nm; (c) PbS NCs were grown at 180 °C for 10 min, average diameter, −3 nm; (d) PbS/TiO_2 films fabrication using a 9-cycle CBD method; (e) typical EDX spectra of PbS/TiO_2 films comprising 3 nm PbS NCs.

concentrations (PbO/octadecene <0.1 M), as was confirmed by the absence of characteristic Bragg lines in the XRD spectra (not shown), and was enabled when the concentration of PbO in octadecene (ODE) exceeded ~0.23 M. Surprisingly, further increases in the precursor concentration resulted primarily in the increasing density of PbS sites and only minor growth of the average PbS diameter (Figures 3a,d). Overall, the comparison of different synthetic conditions, summarized in Figure 3, indicates that ligand-induced control of the NC shape appears to be the most effective mechanism for tuning the diameter of substrate-bound PbS domains.

The lattice structure of PbS domains was further investigated using X-ray powder diffraction (XRD). Figure 4 shows several examples of XRD spectra corresponding to PbS/TiO_2 nanocomposites grown using different synthetic conditions and comprising small-diameter (d = 3.0 nm, trace a) and large-diameter (d = 4.7 nm, trace c) PbS NCs. In all of the observed spectra, the diffraction patterns contained distinct sets of anatase TiO_2 and rock-salt PbS Bragg peaks, with smaller-diameter PbS NCs having relatively wider line widths, as expected from the Scherrer formula.[78] In the case of 3.0-nm PbS NCs, the measured XRD pattern was found to be similar to the diffraction pattern of PbS/TiO_2 films grown *via* a 9-cycle CBD method (Figure 4d), as judged from the comparison of widths and relative intensities of (200) and (220) PbS Bragg lines. This result indicates that 3.0-nm PbS NCs in hot-injection films are nearly identical to those in CBD-grown films both in terms of

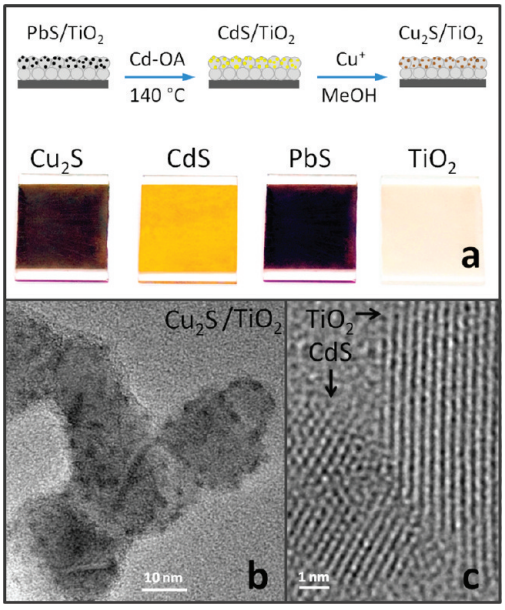

Figure 5. (a) Images of NC/oxide films after Pb→Cd and Pb→Cu cation exchange performed on PbS/TiO_2 substrates; (b) a typical TEM image of Cu_2S/TiO_2 film fragment; (c) high resolution TEM image of a CdS/TiO_2 heterostructure.

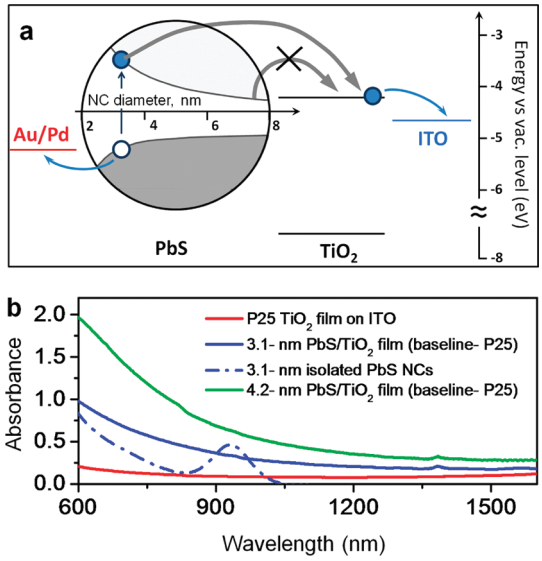

Figure 6. (a) Energy diagram showing a relative alignment of the conduction and valence band edges in PbS/TiO_2 heterostructures. According to the expected relationship between the energy of 1Se (PbS) state and the nanocrystal size, the photoinduced electron transfer from PbS to TiO_2 domain is allowed only if the diameter of PbS NCs is less than 7 nm. (b) Absorption spectra of PbS/TiO_2 films comprising 3.1 and 4.2 nm PbS NCs. The absorption spectrum of annealed TiO_2 films (P-25, Degussa) on ITO was used as a baseline.

the average nanoparticle size and the overall crystal quality. On the other hand, the PbS Bragg lines corresponding to 4.7-nm PbS/TiO_2 films (grown at 180 °C, Figure 3b) are narrower and stronger in intensity than those of CBD-grown PbS NCs. Relatively smaller widths of Bragg peaks in trace b indicates that the hot-injection method can enable the growth of PbS NCs with diameters larger than multicycle CBD approach, for which the average size ranges from 2.5 to 3.5 nm.[20] Furthermore, since the ratio of Pb to Ti elements in 3.0-nm PbS/TiO_2 films is the same as in 4.7-nm PbS/TiO_2, as judged by EDX measurements, the stronger intensity of 200 and 220 PbS Bragg lines observed for 4.7-nm PbS NCs cannot be solely attributed to the increased volume of PbS material in these films, and is believed to result from the improved crystallinity of PbS domains. It is also interesting to note that PbS/TiO_2 films grown at elevated temperatures (T = 280 °C) show markedly increased PbS XRD intensities (Figure 3a) as compared to nanocomposites grown at 180 °C (Figure 3b). Since the average size of PbS domains grown at 280 °C is approximately the same as that of NCs grown at 180 °C (see Figure 3), the relative increase of XRD intensities in nanocomposites fabricated at 280 °C was attributed to a greater density of PbS NCs on TiO_2. This hypothesis is also confirmed by EDX measurements showing an increased ratio of Pb to Ti elements in PbS/TiO_2 materials grown at 280 °C.

To demonstrate the extendibility of the substrate-bound NC growth to other material system, fabricated PbS/TiO_2 heterostructures were transformed into CdS/TiO_2 and subsequently a Cu_2S/TiO_2 system using $Pb^{2+}\rightarrow Cd^{2+}\rightarrow 2Cu^{+}$ cation exchange. Remarkably, the overall nanoparticle shape does not change during such transformation, making this technique ideal for template-based synthesis of many semiconductor NCs.[79] We found that the direct exchange of cations in PbS using aqueous solutions of Cu, Zn, and Sn ion salts was not very effective leading to only a miniscule fraction of ions being replaced; however, if Pb cations were first exchanged with Cd *via* hot-temperature protocols,[80,81] the subsequent $Cd^{2+}\rightarrow 2Cu^{+}$ cation replacement could be performed.

Figure 5 shows a few representative TEM images of heterostructured films fabricated from PbS/TiO_2 substrates *via* cation exchange. The materials were characterized using EDX and XRD to confirm the formation of new crystalline phases, while the shapes of resulting NCs domains were analyzed using HR-TEM images. The size-dispersion of both Cu_2S and CdS NCs was approximately similar to that of starting PbS NCs, as was expected due to the preservation of NC shapes during cation exchange. The biggest challenge faced at this stage was controlling the stoichiometry of resulting NCs/oxide interfaces, as Pb^{2+} cations located at the core of large-diameter NCs (>5 nm) were difficult to replace.

It is expected that optoelectronic properties of PbS/TiO_2 heterostructures are strongly dependent on the average size of PbS domains. According to the excited-state energy diagram[82,83] in Figure 6a, photoinduced electron transfer across PbS/TiO_2 interface is energetically allowed only when the diameter of PbS NCs is less

than ~7 nm. In this case, the staggered alignment of conduction and valence band edges at the PbS/TiO_2 interface creates positive exothermicity that drives the electron transfer reaction. Conversely, for PbS nanoparticles with diameters greater than 7 nm, the PbS/TiO_2 heterostructure exhibits type I alignment of band edges, in which case both excited carriers remain within the PbS material.

Different regimes of the band edge alignment in the PbS/TiO_2 system are reflected in optical properties of these films (Figure 6b). For instance, the absorption profile of PbS/TiO_2 nanocomposites, comprising 3.1-nm (a) and 4.2-nm (b) diameter PbS NCs is characteristic of type II heterostructures with nonzero photon absorption in the spectral range below the band gap of both PbS and TiO_2 materials. In addition to the scattering of light on TiO_2 grains, which contributes an inhomogeneous offset of the absorption curve (Figure 6b, red curve), the observed infrared component contains a low-energy tail, which is attributed to excitations of intermediate states that exist at the junction of PbS and TiO_2 domains.[68] These transitions are commonly observed in heterostructured nanocrystals exhibiting type II carrier confinement and could be beneficial to both photovoltaic and photocatalytic applications of PbS/TiO_2 nanocomposites, as they red-shift the absorption range of PbS/TiO_2 films by several hundreds of nanometers, compared to isolated PbS NCs. Notably, despite a relatively small dispersion of PbS sizes (<11%) the 1S(e)−1S(h) excitonic peak could not be distinguished in the absorption spectra of PbS/TiO_2 films. The observed suppression of excitonic features in heteroepitaxial semiconductor NCs has been observed previously for ZnSe@CdS,[66] CdTe/CdSe,[61,84] and PbSe/TiO_2[74] systems and is believed to arise due to the delocalization of excited carriers across the two domains.

To estimate the potential of fabricated nanocomposite substrates for energy conversion *via* charge separation process, PbS/TiO_2 films were incorporated as a working electrode into a prototype solar cell, comprising a solid hole-transporting layer. The latter was fabricated by spincoating a thin layer of isolated PbS NCs, interlinked with short 3-mercaptopropionic acid (MPA) ligands on top of a PbS/TiO_2 film using a methodology reported in ref 85. The effectiveness of such MPA-PbS arrays as a hole conducting medium has been recently demonstrated through a depleted heterojunction (DH) solar cell architecture, where impressive values of PCE, ranging from 3 to 5.1% have been reported.[85,86] On the basis of the length of MPA molecules, we anticipate that the hole mobility, μ_h, of MPA−PbS films is comparable to that of commonly used 1,2-ethanedithiol (EDT)-interlinked PbS films,[87] for which μ_h = 0.028 $cm^2\ V^{-1}\ s^{-1}$ were reported.[88] In the present work, we employ a 140−200 nm film of monodisperse, MPA-capped PbS NCs for the re-

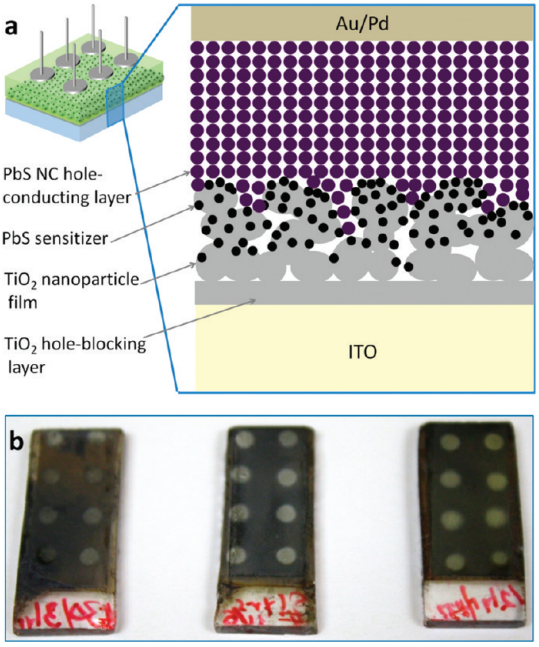

Figure 7. (a) Schematics of the AI-NCSSC device comprising ITO-covered glass, PbS/TiO_2 film, and PbS NC hole-conducting layer; (b) an image showing typical AI-NCSSC cells comprising eight 0.03-cm^2 Au/Pd counter electrodes.

generation of photoinduced holes in PbS/TiO_2 nanocomposite films, which gives rise to an all-inorganic NC-sensitized solar cell (AI-NCSSC) design. It should be stressed that despite relying on the same hole-conducting layer, the present AI-NCSSC scheme is yet conceptually different from the DH architecture. Indeed, upon illumination of AI-NCSSC cells from the TiO_2 side of the device, most of the light (>90% @ λ = 750 nm, >99% @ λ = 600 nm, Figure 6b) becomes absorbed by the epitaxially grown PbS domains, leaving only a fraction of the visible incident flux (<1%, for λ < 600 nm) to penetrate into the hole-conducting array of isolated PbS NCs. This percentage is greater for the infrared portion of the solar radiation since the band gap of matrix PbS NCs is smaller than that of TiO_2-bound nanoparticles. The absorbance spectrum in Figure 6b also indicates that the PbS NC array in a AI-NCSSC configuration functions primarily as a hole conductor and not the light absorber component (since the light is mostly absorbed by the sensitizer), which allows a reduction of the thickness of the PbS array layer relative to that of a DH cell architecture. A thinner NC matrix should result in a decreased probability of hole trapping at unpassivated surfaces of PbS NCs, potentially enhancing the short circuit current of the device.

The schematics of fabricated AI-NCSSC solar cells utilizing PbS/TiO_2 nanocomposites are shown in Figure 7a. Prior to the deposition of the TiO_2 paste, ITO slides were treated with $TiCl_4$ to form a dense oxide film that served as a hole-blocking layer. The hole-conducting layer was made of monodisperse 4.4-nm PbS NCs

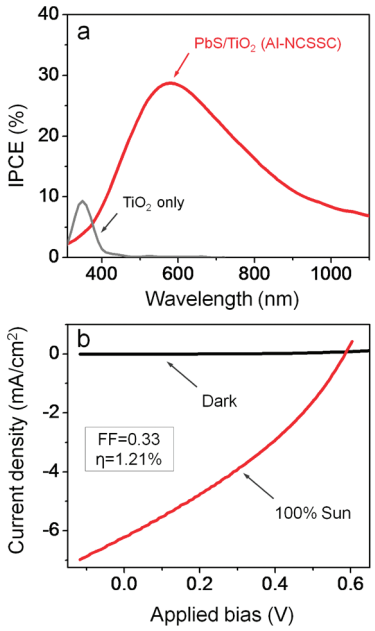

Figure 8. (a) IPCE spectra of AI-NCSSC cells comprising PbS/TiO_2 nanocomposite films (red) and TiO_2 only (gray); (b) *J*−*V* measurements of the best-performing AI-NCSSC cell.

fabricated according to ref 85 and was deposited on top of PbS/TiO_2 films *via* 5−12 cycles of sequential spin coating and three mercaptopropionic acid (MPA) treatment steps. To complete the cell assembly, 0.03-cm^2, Au/Pd contacts were sputtered on top of a PbS hole-conducting layer through a shadow mask.

Figure 8 shows the incident-photon-to-electron conversion efficiency (IPCE) and *J*−*V* response of the best-performing AI-NCSSC cell comprising ~3.3-nm PbS sensitizer NCs and fabricated using the above-mention procedure (ITO/PbS/TiO_2/4.4 nm-PbS/Au/Pd). The measured IPCE curve resembles the absorption profile of PbS/TiO_2 films (Figure 6b) in the short-wavelength range (350 nm < λ < 520 nm), reaching the maximum of 29% (λ = 585 nm) and tails off at λ > 1100 nm, where the quantum efficiency drops below 10%. The decrease of the photocurrent at longer wavelengths can be partly attributed to the existence of an activation energy threshold at the PbS/TiO_2 interface, which decreases the rate of photoinduced electron transfer for low energy electrons. Using the AM1.5 *J*−*V* curve of the best-performing device, we have determined the fill factor (FF) to be 0.33, which corresponds to the PCE value of 1.21%. Remarkably, the measured PCE is comparable or greater than the best reported PCE values of NC-sensitized solar cells (0.8−1.25%),[20] fabricated *via* conventional CBD growth of the PbS sensitizer. On the other hand, it is still lower than the efficiency of depleted-heterojunction devices reported in ref 85. Nevertheless, due to the distinct advantages offered by the demonstrated substrate-bound NC growth and ensuing cell design (thinner hole-conducting layer and all-inorganic, epitaxial heterojunction) we

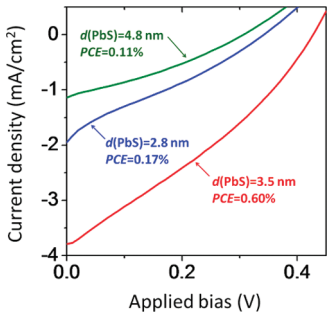

Figure 9. *J*−*V* measurements of AI-NCSSC devices comprising PbS/TiO_2 films with different diameters of epitaxial PbS NCs.

anticipate that the optimized device, emerging as a result of the future work, will show improved characteristics.

The effect of the nanocrystal size on the efficiency of AI-NCSSC solar cells is illustrated in Figure 9. In these experiments, AI-NCSSC cells were prepared using three different PbS/TiO_2 working electrode morphologies, comprising 2.8, 3.5, and 4.8 nm PbS NCs, and were subsequently used to measure the corresponding *J*−*V* curves. The average size of isolated PbS NCs within a hole-conducting layer was maintained at d = 4.4 nm for all three devices. According to Figure 9, the best efficiency was obtained for films with 3.5 nm PbS NCs, indicating that a relatively weak absorption of these NCs in the red portion of the solar spectrum is partly compensated by the optimally positioned edge of the valence band (Figure 6a), which allows for an efficient injection of photoinduced holes into 4.4 nm PbS NCs of the hole-conducting layer.[89] On the other hand, when the size of epitaxial PbS NCs exceeded the diameter of isolated PbS NCs in the matrix (d = 4.8 nm, green curve), the injection of photoinduced holes into the PbS NC array became suppressed, and the efficiency of the cell dropped to 0.11%, despite a significant overlap of NC absorption and solar emission spectral profiles in this case. In principle, it should be possible to achieve greater efficiencies with large-size PbS NCs on TiO_2, provided that the hole-conducting layer is made of isolated NCs with even larger diameters. Finally, in the case of 2.8 nm epitaxial PbS NCs, the relatively low efficiency (PCE = 0.17%) is explained due to relatively poor absorption of the NCs across the solar spectrum, and nonoptimal alignment of valence band edges with the hole-conducting layer.

Figure 10a describes the relationship between the efficiency of AI-NCSSC cells and the thickness of the PbS hole-conducting layer. As was mentioned above, AI-NCSSC design employs such layers primarily as a charge-transporting component, which does not contribute significantly into the absorption of light. Therefore, the thickness of the PbS matrix can potentially be reduced relative to that of DH architecture. This hypothesis is supported by measurements summarized

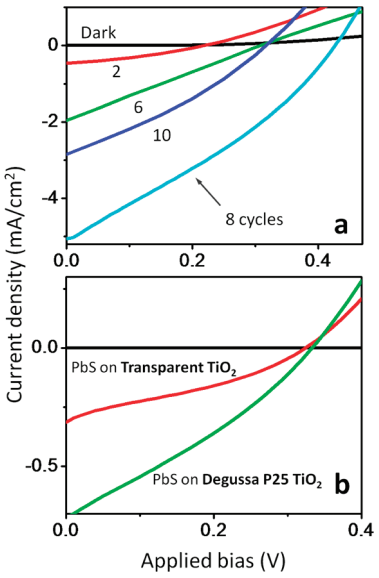

Figure 10. (a) Comparison of the *J*–*V* curves for Al-NCSSC cells comprising different thicknesses of the PbS hole-conducting layer. The number next to the curve represents the amount of spin-coating cycles that were used for the deposition of the PbS matrix. The efficiency of the cell is maximized after approximately eight deposition cycles. (b) *J*–*V* measurements of Al-NCSSC cells comprising transparent (red curve) and P25 Degussa (green curve) TiO_2 films.

in Figure 10, showing that the maximum performance of an Al-NCSSC device is realized after approximately 8 deposition cycles, involving sequential steps of NC spin-coating and MPA interlinking, while the average number of deposition cycles determined for a DH cell using the same concentration of PbS inks is 12.

The analysis in Figure 10a identifies some of the issues limiting the performance of fabricated Al-NCSSC devices. On one hand, the deposition of too few layers of the PbS matrix in a Al-NCSSC cell results in a lower fill factor, which, judging by the constant slope of the *J*–*V* curve leads to a low shunt resistance of the cell assembly. On the other hand, the deposition of too many PbS layers increases the in-series resistance of the cell, as manifested by the lower value of I_{SC} and the corresponding change of the *J*–*V* slope at the *y*-intercept. Furthermore, according to the *J*–*V* profile of the best performing cell (Figure 8b), exhibiting nearly constant $\Delta J/\Delta V$ value across the *V* axis, the negative effect of the low shunt resistance cannot be effectively reduced by increasing the number of PbS deposition cycles as this would enhance the in-series resistance of the cell (see Figure 10a). Consequently, the competition of the two above-mentioned contributions into the cell resistance results in lower values of FF in fabricated devices. Further research aimed toward the improvement of the hole-conducting layer may be needed to address these limitations. Finally, in regard to the effect of the TiO_2 film morphology on cell performance, we have compared the *J*–*V* curves of the two Al-NCSSC cells comprising homemade, transparent TiO_2 paste, and commercial TiO_2 nanoparticle paste from Degussa (Figure 10b). In all of the performed experiments, Degussa TiO_2-based PbS/TiO_2 films yielded consistently better FF and PCE values.

CONCLUSIONS

In summary, we have developed a simple chemical method for coupling colloidal NCs on TiO_2 substrate films *via* hot-injection routes. The reported technique is enabled by introducing a thin layer of substrate-bound oxide into the reaction flask prior to the injection of organometallic precursors, which leads to the formation of NC/TiO_2 nanocomposites exhibiting a fully inorganic interface between semiconductor and oxide domains. Using a PbS/TiO_2 material combination as a model system, we demonstrate that the reported substrate-bound NC growth technique results in a narrow distribution of NC sizes and good crystalline quality, which compares favorably to NCs fabricated on TiO_2 substrates *via* traditional SILAR or CBD methods. The extendibility of the present method to other material systems is demonstrated here through the synthesis of lead, cadmium, and copper chalcogenide NCs on TiO_2 substrates. The light-harvesting performance of fabricated PbS/substrate composites was demonstrated by constructing prototype solar cells, for which the maximum power conversion efficiency of 1.2% was observed.

From the synthetic standpoint, the present method of growing semiconductor NCs in a substrate-bound form provides a facile strategy for achieving an efficient electronic coupling between colloidally grown NCs and the substrate material. We anticipate that this approach can be extended to other nanocrystal/substrate material combinations, thus opening new opportunities for the development of heterostructured films from solutions to be used in new-generation photovoltaic, photocatalytic, and light-emitting devices.

METHODS

Materials. 1-Octadecene (ODE, 90% Aldrich), oleylamine (OLAM, 70% Aldrich), oleic acid (OA, 90% Aldrich), titanium tetrachloride ($TiCl_4$, 99.9% Aldrich), titanium(IV) isopropoxide (99.999%, Aldrich), lead(II) nitrate ($Pb(NO_3)_2$, 99.99% Aldrich), lead(II) oxide powder (PbO, 99.999% Aldrich), sodium sulfide nonanhydrate ($Na_2S.9H_2O$, 98% Alfa Aesar), sulfur (S, 99.999% Acros), titanium dioxide (P25, Evonick Degussa), selenium powder (Se, 99.5% Acros), tellurium powder (Te, 99.8% Aldrich), ethanol (anhydrous, 95% Aldrich), methanol (anhydrous, 99.8%

Aldrich), toluene (anhydrous, 99.8% Aldrich), isopropyl alcohol (anhydrous, 99.8% Acros), octane (anhydrous, 99% Aldrich), 3-mercaptopropionic acid (3-MPA, 99% Alfa Aesar), bis-(trimethylsilyl) sulfide (TMS, Aldrich, synthetic grade), tri-n-octylphosphine (97%, Strem), and Triton X-100 (Alfa Aesar) were used as received without any further purification. Regular acetone was distilled before using, and all reactions were performed under argon atmosphere using the standard Schlenk technique. ITO glass (TEC 15, 12−14 Ohm/sq) was obtained from Pilkington Glass.

Preparation of TiO_2 films on ITO/Glass. ITO glass was cut into 1 cm × 2.5 cm slides so that it could be inserted into a 14/20 size three-neck flask. The ITO substrate was first cleaned with toluene and subsequently sonicated in a 2% solution of triton in deionized water for 10 min and then in a mixture of isopropyl alcohol and deionized water for an additional 10 min and finally dried. TiO_2 paste was made by sonicating a mixture of 1.75 g of TiO_2 nanoparticles (Degussa, P25) and 7.5 mL ethanol for 40 min. Subsequently, 0.25 mL of titanium tetraisopropoxide was added, and the mixture was sonicated further to form a homogeneous paste. Transparent TiO_2 paste was prepared according to the procedure in ref 90. A TiO_2 paste was doctor-bladed onto ITO-coated glass surface and sintered at 450 °C for 30 min to allow good electronic conduction. For the growth of PbS NCs onto the film, two TiO_2/ITO glass slides were attached facing each other (1 mm spacer was used), which allowed reactants to flow across film surfaces, while preventing any scratching of the film due to stirring.

Preparation of Injection Precursors. For the growth of PbS NCs, the lead precursor was prepared by dissolving 1.6 g (7.2 mmol) of PbO in a mixture of 2.9 g of OA and 4 g of ODE by heating the flask to 180 °C for 1 h. A sulfur solution was prepared by heating 0.20 g (6.2 mmol) of S in 2.4 g of ODE at 200 °C for 2 min and cooling the flask down to room temperature. For PbSe NC growth, lead precursor was prepared by dissolving 0.45 g (2.0 mmol) of lead oxide in a mixture of 1.6 g of OA and 4 g of ODE by heating the flask to 180 °C. TOP−Se solution was prepared by sonicating 0.21 g of Se in 2.24 g of TOP at room temperature. For PbTe NC growth, 0.225 g (1.0 mmol) PbO was dissolved in 1.89 g OA and 4.7 g ODE at 180 °C, and Te precursor was prepared by sonicating 0.063 g (0.5 mmol) Te powder in 0.83 g TOP until a clear solution was obtained.[91]

Growth of PbS, PbSe, and PbTe NCs on a TiO_2 Film. A 2.85 g portion of OLAM was degassed in a three-neck 50-ml flask at 120 °C for half an hour, at which point the flask was switched to argon and the reaction mixture was allowed to cool to room temperature. At this stage, a substrate with TiO_2 films was carefully inserted into the flask and the temperature was raised to 180 °C. To initiate the growth of PbS NCs, lead oleate (at 180 °C) and sulfur (at room temperature) were injected quickly. After the temperature recovered to 180 °C (2 min), the flask was heated for an additional 8−17 min and subsequently raised from the mantle. To ensure that isolated PbS NCs are completely removed from the sample upon completion of the synthesis, the PbS/TiO_2 film was repeatedly washed with toluene until the changes in its absorption profile became negligible. PbSe and PbTe NCs were grown using the same procedure by injecting respective precursors.

Synthesis of CdS/PbS and Cu_2S/PbS. To initiate the $Pb^{2+} \rightarrow Cd^{2+}$ cation exchange in fabricated PbS/TiO_2 films, substrates were lowered into a cadmium stock solution prepared by dissolving 1 g of CdO in 6 mL of OA and 15 mL of ODE. The exchange proceeded at 120−140 °C for 15−20 min, upon which the substrate was removed from the flask and washed with toluene. CdS/TiO_2 films were subsequently converted to Cu_2S/TiO_2 using the previously described room-temperature addition of new cations.[92] In a typical reaction, the ion exchange stock solution was prepared by dissolving 10 mg of tetrakis(acetonitrile)-copper(I) hexafluorophosphate $[MeCN]_4Cu^IPF_6$ in 2 mL of 1:1 methanol/toluene solvent mixture. The CdS/TiO_2 film was treated with the ion exchange stock solution through drop by drop addition of the latter to a spinning substrate. The cation replacement could be visibly confirmed through the change in the color of the film from yellow to brown. Cleaning of the substrate was done in methanol.

Synthesis of Isolated PbS NCs for a Hole-Conducting Layer. PbS NCs were fabricated according to a procedure adapted from ref 76. In a typical synthesis, a mixture of 0.45 g PbO, 14.04 g ODE, and 1.34 g OA was degassed in a three-neck flask at 120 °C for 5 h and switched to argon. In the other flask, 10 mL of ODE was degassed for 2 h at 120 °C and allowed to cool down to room temperature, then 0.18 g of TMS was added carefully into the flask containing ODE and the resulting TMS/ODE mixture was injected into the Pb precursor solution at 120 °C, while stirring. The color of the mixture immediately turned black. After 1−2 min, the reaction was quenched by removing the flask from the heating mantle and placing it in ice-cold water. One minute of the growth time generally yielded PbS NCs with 4.0−4.4 nm diameter. The NC mixture was cleaned by precipitating the reaction product with 60 mL of acetone and redissolving the precipitate in toluene. The mixture was precipitated again using 20 mL of acetone and finally redissolved in 2 mL of octane to make a stock solution. The required concentration of PbS NCs was obtained by diluting the stock solution with octane.

Deposition of the Hole-Conducting Layer and Au/Pd Counter Electrodes. Before the deposition of the hole-conducting layer, a PbS/TiO_2 nanocomposite film was treated with 5 drops of 3-MPA twice, followed by washing with 10 drops of methanol and octane each. The hole-conducting matrix of PbS NCs was deposited layer by layer *via* sequential cycles of spin coating of PbS NCs and 3-MPA at 1500 rpm, according to ref 85. Briefly, 4 drops of 37 mg/mL PbS NCs in octane, 5 drops 3-MPA and methanol (1:9), 10 drops of anhydrous methanol, and 10 drops of anhydrous octane were added sequentially on each cycle without stopping the substrate. The number of cycles that optimizes the solar cell performance was eight. Finally, to complete the cell assembly, 15 nm of gold−palladium (Au−Pd, 40/60) counter electrodes were coated on top of the film using Polaron E500 sputter, which was equipped with a 2-mm diameter shadow mask generating eight pixels in each device.

Characterization. Absorbance spectra were recorded using CARY 50 scan and Simadzu UV-3600 UV−vis−NIR spectrophotometers. High-resolution transmission electron microscopy (HR-TEM) measurements were carried out using JEOL 3011UHR and 2010 transmission electron microscopes, operated at 300 and 200 kV, respectively. To prepare a TEM sample, a small amount of PbS/TiO_2 nanocomposite film was scraped, dispersed in toluene by sonication, dropped onto a carbon-coated copper grid, and allowed to dry in air. X-ray powder diffraction (XRD) measurements were carried out on a Scintag XDS-2000 X-ray powder diffractometer. Energy dispersive X-ray (EDX) emission spectra were measured using an EDAX X-ray detector located inside the *Inspect* scanning electron microscope (SEM). The electron beam was accelerated at 10 kV. Current−voltage characteristics were performed under AM 1.5 G (100 mW/cm^2) solar simulator using *I*−*V* data acquisition system from PV Measurements, Inc., while, the incident photon to charge carrier efficiency (IPCE) was measured using a home-build system comprising a xenon lamp, a CM110 1/8 m monochromator, and a SR-830 lock-in amplifier.

Acknowledgment. We would like to acknowledge Dr. Felix Castellano (BGSU) for advice and valuable discussions. We gratefully acknowledge OBOR "Material Networks" program and Bowling Green State University for financial support.

Supporting Information Available: Additional TEM and HRTEM images. This material is available free of charge *via* the Internet at http://pubs.acs.org.

REFERENCES AND NOTES

1. Klimov, V. I.; Mikhailovsky, A. A.; Xu, S.; Malko, A.; Hollingsworth, J. A.; Leatherdale, C. A.; Bawendi, E. H. Optical Gain and Stimulated Emission in Nanocrystal Quantum Dots. *Science* **2000**, *290*, 314–317.
2. Klimov, V. I. Mechanisms for Photogeneration and Recombination of Multiexcitons in Semiconductor Nanocrystals:

Implications for Lasing and Solar Energy Conversion. *J. Phys. Chem. B* **2006**, *110*, 16827–16845.
3. Klimov, V. I.; Ivanov, S. A.; Nanda, J.; Achermann, M.; Bezel, I.; McGuire, J. A.; Piryatinski, A. Single-Exciton Optical Gain in Semiconductor Nanocrystals. *Nature* **2007**, *447*, 441–446.
4. Hillhouse, H. W.; Beard, M. C. Solar Cells from Colloidal Nanocrystals: Fundamentals, Materials, Devices, and Economics. *Curr. Opin. Colloid Interface Sci.* **2009**, *14*, 245–259.
5. Huynh, W. U.; Dittmer, J. J.; Alivisatos, A. P. Hybrid Nanorod–Polymer Solar Cells. *Science* **2002**, *295*, 2425–2427.
6. McDonald, S. A.; Konstantatos, G.; Zhang, S.; Cyr, P. W.; Klem, E. J. D.; Levina, L.; Sargent, E. H. Solution-Processed PbS Quantum Dot Infrared Photodetectors and Photovoltaics. *Nat. Mater.* **2005**, *4*, 138–142.
7. Ellingson, R. J.; Beard, C. M.; Johnson, J. C.; Yu, P.; Micic, O. I.; Nozik, A. J.; Shabaev, A.; Efros, A. L. Highly Efficient Multiple Exciton Generation in Colloidal PbSe and PbS Quantum Dots. *Nano Lett.* **2005**, *5*, 865–871.
8. Maria, A.; Cyr, P. W.; Klern, E. J. D.; Levina, L.; Sargent, E. H. Solution-Processed Infrared Photovoltaic Devices with >10% Monochromatic Internal Quantum Efficiency. *Appl. Phys. Lett.* **2005**, *87*, 213112.
9. Kim, S. J.; Kim, W. J.; Cartwright, A. N.; Prasad, P. N. Carrier Multiplication in a PbSe Nanocrystal and P3HT/PCBM Tandem Cell. *Appl. Phys. Lett.* **2008**, *92*, 191107.
10. Gur, I.; Fromer, N. A.; Geier, M. L.; Alivisatos, A. P. Air-Stable All-Inorganic Nanocrystal Solar Cells Processed from Solution. *Science* **2005**, *310*, 462–465.
11. Guo, Q.; Kim, S. J.; Kar, M.; Shafarman, W. N.; Birkmire, R. W.; Stach, E. A.; Agrawal, R.; Hillhouse, H. W. Development of $CuInSe_2$ Nanocrystal and Nanoring Inks for Low-Cost Solar Cells. *Nano Lett.* **2008**, *8*, 2982–2987.
12. Leschkies, K. S.; Beatty, T. J.; Kang, M. S.; Norris, D. J.; Aydil, E. S. Solar Cells Based on Junctions between Colloidal PbSe Nanocrystals and Thin ZnO Films. *ACS Nano* **2009**, *3*, 3638–3648.
13. Ma, W.; Luther, J. M.; Zheng, H.; Wu, Y.; Alivisatos, A. P. Photovoltaic Devices Employing Ternary PbS_xSe_{1-x} Nanocrystals. *Nano Lett.* **2009**, *9*, 1699–1703.
14. Lee, H. J.; Yum, J.-H.; Leventis, H. C.; Zakeeruddin, S. M.; Haque, S. A.; Chen, P.; Seok, S. I.; Grätzel, M.; Nazeeruddin, M. K. CdSe Quantum Dot-Sensitized Solar Cells Exceeding Efficiency 1% at Full-Sun Intensity. *J. Phys. Chem. C* **2008**, *112*, 11600–11608.
15. Hao, E. C.; Yang, B.; Zhang, J. H.; Zhang, X.; Sun, J. Q.; Shen, S. C. Assembly of Alternating TiO_2/CdS Nanoparticle Composite Films. *J. Mater. Chem.* **1998**, *8*, 1327–1328.
16. Mora-Sero, I.; Bisquert, J.; Dittrich, T.; Belaidi, A.; Susha, A. S.; Rogach, A. L. Photosensitization of TiO_2 Layers with CdSe Quantum Dots: Correlation between Light Absorption and Photoinjection. *J. Phys. Chem. C* **2007**, *111*, 14889–14892.
17. Yu, P. R.; Zhu, K.; Norman, A. G.; Ferrere, S.; Frank, A. J.; Nozik, A. J. Nanocrystalline TiO_2 Solar Cells Sensitized with InAs Quantum Dots. *J. Phys. Chem. B* **2006**, *110*, 25451–25454.
18. Vogel, R.; Hoyer, P.; Weller, H. Quantum-Sized PbS, CdS, Ag_2S, Sb_2S_3, and Bi_2S_3 Particles as Sensitizers for Various Nanoporous Wide-Bandgap Semiconductors. *J. Phys. Chem.* **1994**, *98*, 3183.
19. Hoyer, P.; Konenkamp, R. Photoconduction in Porous TiO_2 Sensitized by PbS Quantum Dots. *Appl. Phys. Lett.* **1995**, *66*, 349–351.
20. Lee, H.; Leventis, H. C.; Moon, S.-J.; Chen, P.; Ito, S.; Haque, S. A.; Torres, T.; Nüesch, F.; Geiger, T.; Zakeeruddin, S. M.; *et al*. PbS and CdS Quantum Dot-Sensitized Solid-State Solar Cells: "Old Concepts, New Results.. *Adv. Funct. Mater.* **2009**, *19*, 2735–2742.
21. Lee, L.; Wang, M.; Chen, P.; Gamelin, D. R.; Zakeeruddin, S. M.; Grätzel, M.; Nazeeruddin, M. K. Efficient CdSe Quantum Dot-Sensitized Solar Cells Prepared by an Improved Successive Ionic Layer Adsorption and Reaction Process. *Nano lett.* **2009**, *9*, 4221–4227.
22. Oregan, B.; Grätzel, M. A Low-Cost, High-Efficiency Solar Cell Based on Dye-Sensitized Colloidal TiO_2 Films. *Nature* **1991**, *353*, 737–740.
23. Kamat, P. V.; Flumiani, M.; Dawson, A. Metal–Metal and Metal–Semiconductor Composite Nanoclusters. *Colloids Surf. A* **2002**, *202*, 269–279.
24. Dawson, A.; Kamat, P. V. Semiconductor–Metal Nanocomposites. Photoinduced Fusion and Photocatalysis of Gold-Capped TiO_2 (TiO_2/Gold) Nanoparticles. *J. Phys. Chem. B* **2001**, *105*, 960–966.
25. Borensztein, Y.; Delannoy, L.; Djedidi, A.; Barrera, R. G.; Louis, C. Monitoring of the Plasmon Resonance of Gold Nanoparticles in Au/TiO_2 Catalyst under Oxidative and Reducing Atmospheres. *J. Phys. Chem. C* **2010**, *114*, 9008–9021.
26. Amirav, L.; Alivisatos, A. P. Photocatalytic Hydrogen Production with Tunable Nanorod Heterostructures. *J. Phys. Chem. Lett.* **2010**, *1*, 1051–1054.
27. Coe, S.; Woo, W. K.; Bawendi, M.; Bulovic, V. Electroluminescence from Single Monolayers of Nanocrystals in Molecular Organic Devices. *Nature* **2002**, *420*, 800–803.
28. Tessler, N.; Medvedev, V.; Kazes, M.; Kan, S. H.; Banin, U. Efficient Near-Infrared Polymer Nanocrystal Light-Emitting Diodes. *Science* **2002**, *295*, 1506–1508.
29. Steckel, J. S.; Snee, P.; Coe-Sullivan, S.; Zimmer, J. R.; Halpert, J. E.; Anikeeva, P.; Kim, L. A.; Bulovic, V.; Bawendi, M. G. Color-Saturated Green-Emitting QD-LEDs. *Angew Chem. Int. Ed.* **2006**, *45*, 5796–5799.
30. Colvin, V. L.; Schlamp, M. C.; Alivisatos, A. P. Light-Emitting Diodes Made from Cadmium Selenide Nanocrystals and a Semiconducting Polymer. *Nature* **1994**, *370*, 354–357.
31. Schlamp, M. C.; Peng, X. G.; Alivisatos, A. P. Improved Efficiencies in Light Emitting Diodes Made with CdSe(CdS) Core/Shell Type Nanocrystals and a Semiconducting Polymer. *J. Appl. Phys.* **1997**, *82*, 5837–5842.
32. Mattoussi, H.; Radzilowski, L. H.; Dabbousi, B. O.; Thomas, E. L.; Bawendi, M. G.; Rubner, M. F. Electroluminescence from Heterostructures of Poly(phenylene vinylene) and Inorganic CdSe Nanocrystals. *J. Appl. Phys.* **1998**, *83*, 7965–7974.
33. Sun, Q.; Y. Wang, A. Y.; Li, L. S.; Wang, D.; Zhu, T.; Xu, J.; Yang, C.; Li, Y. Bright, Multicoloured Light-Emitting Diodes Based on Quantum Dots. *Nat. Photon.* **2007**, *1*, 717–722.
34. Caruge, J. M.; Halpert, J. E.; Wood, V.; Bulovic, V.; Bawendi, M. G. Colloidal Quantum-Dot Light-Emitting Diodes with Metal-Oxide Charge Transport Layers. *Nat. Photon.* **2008**, *2*, 247–250.
35. Medintz, I. L.; Uyeda, H. T.; Goldman, E. R.; Mattoussi, H. Quantum Dot Bioconjugates for Imaging, Labelling and Sensing. *Nat. Mater.* **2005**, *4*, 435–446.
36. Bruchez, M.; Moronne, M.; Gin, P.; Weiss, S.; Alivisatos, A. P. Semiconductor Nanocrystals as Fluorescent Biological Labels. *Science* **1998**, *281*, 2013–2016.
37. Mattoussi, H.; Mauro, J. M.; Goldman, E. R.; Anderson, G. P.; Sundar, V. C.; Mikulec, F. V.; Bawendi, M. G. Self-Assembly of CdSe–ZnS Quantum Dot Bioconjugates Using an Engineered Recombinant Protein. *J. Am. Chem. Soc.* **2000**, *122*, 12142–12150.
38. Wang, R. Y.; Feser, J. P.; Lee, J. S.; Talapin, D. V.; Segalman, R.; Majumdar, A. Enhanced Thermopower in PbSe Nanocrystal Quantum Dot Superlattices. *Nano Lett.* **2008**, *8*, 2283–2288.
39. Kovalenko, M. V.; Scheele, M.; Talapin, D. V. Colloidal Nanocrystals with Molecular Metal Chalcogenide Surface Ligands. *Science* **2009**, *324*, 1417–1420.
40. Ridley, B. A.; Nivi, B.; Jacobson, J. M. All-Inorganic Field Effect Transistors Fabricated by Printing. *Science* **1999**, *286*, 746–749.
41. Lee, S.; Jeong, S.; Kim, D.; Park, B. K.; Moon Fabrication of a Solution-Processed Thin-film Transistor Using Zinc Oxide Nanoparticles and Zinc Acetate. *J. Superlattices Microstruct.* **2007**, *42*, 361–368.
42. Schneider, J. J.; Hoffmann, R. C.; Engstler, J.; Soffke, O.; Jaegermann, W.; Issanin, A.; Klyszcz, A. A Printed and Flexible Field-Effect Transistor Device with Nanoscale Zinc

Oxide as Active Semiconductor Material. *Adv. Mater.* **2008**, *20*, 3383–3387.
43. Talapin, D. V.; Mekis, I.; Gotzinger, S.; Kornowski, A.; Benson, O.; Weller, H. CdSe/CdS/ZnS and CdSe/ZnSe/ZnS Core–Shell–Shell Nanocrystals. *J. Phys. Chem. B* **2004**, *108*, 18826–18831.
44. Talapin, D. V.; Murray, C. B. PbSe Nanocrystal Solids for n- and p-Channel Thin Film Field-Effect Transistors. *Science* **2005**, *310*, 86–89.
45. Lee, J. S.; Shevchenko, E. V.; Talapin, D. V. Au–PbS Core–Shell Nanocrystals: Plasmonic Absorption Enhancement and Electrical Doping *via* Intraparticle Charge Transfer. *J. Am. Chem. Soc.* **2008**, *130*, 9673–9675.
46. Erwin, S. C.; Zu, L. J.; Haftel, M. I.; Efros, A. L.; Kennedy, T. A.; Norris, D. J. Doping Semiconductor Nanocrystals. *Nature* **2005**, *436*, 91–94.
47. Salgueirino-Maceira, V.; Correa-Duarte, M. A. Increasing the Complexity of Magnetic Core/Shell Structured Nanocomposites for Biological Applications. *Adv. Mater.* **2007**, *19*, 4131–4144.
48. Son, D. I.; Kim, J. H.; Park, D. H.; Choi, W. K.; Li, F.; Ham, J. H.; Kim, T. W. Nonvolatile Flexible Organic Bistable Devices Fabricated Utilizing CdSe/ZnS Nanoparticles Embedded in a Conducting Poly *N*-vinylcarbazole Polymer Layer. *Nanotechnology* **2008**, *19*, 055204.
49. Liz-Marzan, L. M.; Mulvaney, P. The Assembly of Coated Nanocrystals. *J. Phys. Chem. B* **2003**, *107*, 7312–7326.
50. Das, B. C.; Batabyal, S. K.; Pal, A. J. A Bit per Particle: Electrostatic Assembly of CdSe Quantum Dots as Memory Elements. *Adv. Mater.* **2007**, *19*, 4172–4176.
51. Das, B. C.; Pal, A. J. Memory Applications and Electrical Bistability of Semiconducting Nanoparticles: Do the Phenomena Depend on Bandgap?. *Small* **2008**, *4*, 542–547.
52. Ghosh, B.; Sahu, S.; Pal, A. J. Core–Shell Nanoparticles: An Approach to Enhance Electrical Bistability. *J. Phys. Chem. C* **2008**, *112*, 11290–11294.
53. Peter, L. M.; Riley, D. J.; Tull, E. J.; Wijayantha, K. G. U. Photosensitization of Nanocrystalline TiO_2 by Self-Assembled Layers of CdS Quantum Dots. *Chem. Commun.* **2002**, 1030–1031.
54. Kongkanand, A.; Tvrdy, K.; Takechi, K.; Kuno, M.; Kamat, P. V. Quantum Dot Solar Cells. Tuning Photoresponse through Size and Shape Control of CdSe–TiO_2 Architecture. *J. Am. Chem. Soc.* **2008**, *130*, 4007–4015.
55. Wang, C. J.; Kwon, K. W.; Odlyzko, M. L.; Lee, B. H.; Shim, M. PbSe Nanocrystal/TiO_x Heterostructured Films: A Simple Route to Nanoscale Heterointerfaces and Photocatalysis. *J. Phys. Chem. C* **2007**, *111*, 11734–11741.
56. Hyun, B. R.; Zhong, Y. W.; Bartnik, A. C.; Sun, L.; Abruña, H. D.; Wise, F. W.; Goodreau, J. D.; Matthews, J. R.; Leslie, T. M.; Borrelli, N. F. Electron Injection from Colloidal PbS Quantum Dots into Titanium Dioxide Nanoparticles. *ACS Nano* **2008**, *2*, 2206–2212.
57. Yochelis, S.; Hodes, G. Nanocrystalline CdSe Formation by Direct Reaction between Cd Ions and Selenosulfate Solution. *Chem. Mater.* **2004**, *16*, 2740–2744.
58. Baker, D. R.; Kamat, P. V. Photosensitization of TiO_2 Nanostructures with CdS Quantum Dots: Particulate *versus* Tubular Support Architectures. *Adv. Funct. Mater.* **2009**, *19*, 805–811.
59. Sun, W. T.; Yu, Y.; Pan, H.-Y.; Gao, X.-F.; Chen, Q.; Peng, L. M. CdS Quantum Dots Sensitized TiO_2 Nanotube-Array Photoelectrodes. *J. Am. Chem. Soc.* **2008**, *130*, 1124–1125.
60. Murray, C. B.; Norris, D. J.; Bawendi, M. G. Synthesis and Characterization of Nearly Monodisperse CdE (E = Sulfur, Selenium, Tellurium) Semiconductor Nanocrystallites. *J. Am. Chem. Soc.* **1993**, *115*, 8706–8715.
61. Kim, S.; Fisher, B.; Eisler, H. J.; Bawendi, M. Type-II Quantum Dots: CdTe/CdSe(Core/Shell) and CdSe/ZnTe(Core/Shell) Heterostructures. *J. Am. Chem. Soc.* **2003**, *125*, 11466–11467.
62. Xie, R.; Zhong, X.; Basché, T. Synthesis, Characterization, and Spectroscopy of Type-II Core/Shell Semiconductor Nanocrystals with ZnTe Cores. *Adv. Mater.* **2005**, *17*, 2741–2745.
63. Danek, M.; Jensen, K. F.; Murray, C. B.; Bawendi, M. G. Synthesis of Luminescent Thin-Film CdSe/ZnSe Quantum Dot Composites Using CdSe Quantum Dots Passivated with an Overlayer of ZnSe. *Chem. Mater.* **1996**, *8*, 173–180.
64. Ivanov, S. A.; Piryatinski, A.; Nanda, J.; Tretiak, S.; Zavadil, K. R.; Wallace, W. O.; Werder, D.; Klimov, V. I. Type-II Core/Shell CdS/ZnSe Nanocrystals: Synthesis, Electronic Structures, and Spectroscopic Properties. *J. Am. Chem. Soc.* **2007**, *129*, 11708–11719.
65. Pandey, A.; Guyot-Sionnest, P. Intraband Spectroscopy and Band Offsets of Colloidal II–VI Core/Shell Structures. *J. Chem. Phys.* **2007**, *127*, 104710.
66. Nemchinov, A.; Kirsanova, M.; Hewa-Kasakarage, N. N.; Zamkov, M. Synthesis and Characterization of Type II ZnSe/CdS Core/Shell Nanocrystals. *J. Phys. Chem. C* **2008**, *112*, 9301–9307.
67. Reiss, P.; Protiere, M.; Li, L. Core/Shell Semiconductor Nanocrystals. *Small* **2009**, *5*, 154–168.
68. Hewa-Kasakarage, N. N.; Kirsanova, M.; Nemchinov, A.; Schmall, N.; El-Khoury, P. Z.; Tarnovsky, A. N.; Zamkov, M. Radiative Recombination of Spatially Extended Excitons in (ZnSe/CdS)/CdS Heterostructured Nanorods. *J. Am. Chem. Soc.* **2009**, *131*, 1328–1334.
69. Hewa-Kasakarage, N. N.; Gurusinghe, P. G.; Zamkov, M. Blue-Shifted Emission in CdTe/ZnSe Heterostructured Nanocrystals. *J. Phys. Chem. C* **2009**, *113*, 4362–4368.
70. Shieh, F.; Saunders, A. E.; Korgel, B. A. General Shape Control of Colloidal CdS, CdSe, CdTe Quantum Rods and Quantum Rod Heterostructures. *J. Phys. Chem. B* **2005**, *119*, 8538–8542.
71. Kirsanova, M.; Nemchinov, A.; Hewa-Kasakarage, N. N.; Schmall, N.; Zamkov, M. Synthesis of ZnSe/CdS/ZnSe Nanobarbells Showing Photoinduced Charge Separation. *Chem. Mater.* **2009**, *21*, 4305–4309.
72. Yu, H.; Chen, M.; Rice, P. M.; Wang, S. X.; White, R. L.; Sun, S. Dumbbell-like Bifunctional Au-Fe_3O_4 Nanoparticles. *Nano Lett.* **2005**, *5*, 379–382.
73. Khon, E; Hewa-Kasakarage, N. N.; Nemitz, I; Acharya, K.; Zamkov, M. Tuning the Morphology of Au/CdS Nanocomposites through Temperature-Controlled Reduction of Gold-Oleate Complexes. *Chem. Mater.* **2010**, *22*, 5929.
74. Acharya, K. P.; Alabi, T. R.; Schmall, N.; Hewa-Kasakarage, N. N.; Kirsanova, M.; Nemchinov, A.; Khon, E.; Zamkov, M. Linker-free Modification of TiO_2 Nanorods with PbSe Nanocrystals. *J. Phys. Chem. C* **2009**, *113*, 19531–19535.
75. Acharya, K. P.; Hewa-Kasakarage, N. N.; Alabi, T. R.; Nemitz, I.; Khon, E.; Ullrich, B.; Anzenbacher, P.; Zamkov, M. Synthesis of PbS/TiO_2 Colloidal Heterostructures for Photovoltaic Applications. *J. Phys. Chem. C* **2010**, *114*, 12496–12504.
76. Hines, M. A.; Scholes, G. D. Colloidal PbS Nanocrystals with Size-Tunable Near-Infrared Emission: Observation of Post-synthesis Self-Narrowing of the Particle Size Distribution. *Adv. Mater.* **2003**, *15*, 1844–1849.
77. Rogach, A. L.; Eychmuller, A.; Hickey, S. G.; Kershaw, S. V. Infrared-Emitting Colloidal Nanocrystals: Synthesis, Assembly, Spectroscopy, and Applications. *Small* **2007**, *3*, 536–557.
78. Patterson, A. L. The Scherrer Formula for X-ray Particle Size Determination. *Phys. Rev.* **1939**, *56*, 978–982.
79. Jain, P. K.; Amirav, L.; Aloni, S.; Alivisatos, A. P. Nanoheterostructure Cation Exchange: Anionic Framework Conservation. *J. Am. Chem. Soc.* **2010**, *132*, 9997.
80. Pietryga, J. M.; Werder, D. J.; Williams, D. J.; Casson, J. L.; Schaller, R. D.; Klimov, V. I.; Hollingsworth, J. A. Utilizing the Lability of Lead Selenide to Produce Heterostructured Nanocrystals with Bright, Stable Infrared Emission. *J. Am. Chem. Soc.* **2008**, *130*, 4879–4885.
81. Neo, M. S.; Venkatram, N.; Li, G. S.; Chin, W. S.; Ji, W. Synthesis of PbS/CdS Core–Shell QDs and their Nonlinear Optical Properties. *J. Phys. Chem. C* **2010**, *114*, 18037–18044.
82. Wehrenberg, B. L.; Guyot-Sionnest, P. Electron and Hole Injection in PbSe Quantum Dot Films. *J. Am. Chem. Soc.* **2003**, *125*, 7806–7807.

83. Wei, S. H.; Zunger, A. Electronic and Structural Anomalies in Lead Chalcogenides. *Phys. Rev B* **1997**, *55*, 13605–13610.
84. Koo, B.; Korgel, B. A. Coalescence and Interface Diffusion in Linear CdTe/CdSe/CdTe Heterojunction Nanorods. *Nano Lett.* **2008**, *8*, 2490–2496.
85. Pattantyus-Abraham, A. G.; Kramer, I. J.; Barkhouse, A. R.; Wang, X.; Konstantatos, G.; Debnath, R.; Levina, L.; Raabe, I.; Nazeeruddin, M. K.; Gratzel, M.; *et al.* Depleted-Heterojunction Colloidal Quantum Dot Solar Cells. *ACS Nano* **2010**, *4*, 3374–3380.
86. Ju, T.; Graham, R. L.; Zhai, G.; Rodriguez, Y. W.; Breeze, A. J.; Yang, L.; Alers, G. B.; Sue, A.; Carter, S. A. High Efficiency Mesoporous Titanium Oxide PbS Quantum Dot Solar Cells at Low Temperature. *Appl. Phys. Lett.* **2010**, *97*, 043106.
87. Tang, J.; Sargent, E. H. Infrared Colloidal Quantum Dots for Photovoltaics: Fundamentals and Recent Progress. *Adv. Mater.* **2011**, *23*, 12–29.
88. Liu, Y.; Gibbs, M.; Puthussery, J.; Gaik, S.; Ihly, R.; Hillhouse, H. W.; Law, M. Dependence of Carrier Mobility on Nanocrystal Size and Ligand Length in PbSe Nanocrystal Solids. *Nano Lett.* **2010**, *10*, 1960.
89. Hyun, B. R.; Zhong, Y. W.; Bartnik, A. C.; Sun, L.; Abruña, H. D.; Wise, F. W.; Goodreau, J. D.; Matthews, J. R.; Leslie, T. M.; Borrelli, N. F. Electron Injection from Colloidal PbS Quantum Dots into Titanium Dioxide Nanoparticles. *ACS Nano* **2008**, *2*, 2206.
90. Zaban, A.; Ferrere, S.; Sprague, J.; Gregg, B. A. pH-Dependent Redox Potential Induced in a Sensitizing Dye by Adsorption onto TiO_2. *J. Phys. Chem. B* **1997**, *101*, 55–57.
91. Murphy, J. E.; Beard, M. C.; Norman, A. G.; Ahrenkiel, S. P.; Johnson, J. C.; Yu, P.; Mićić, O. I; Ellingson, R. J.; Nozik, A. J. PbTe Colloidal Nanocrystals: Synthesis, Characterization, and Multiple Exciton Generation. *J. Am. Chem. Soc.* **2006**, *128*, 3241–3247.
92. Sadtler, B.; Demchenko, D. O.; Zheng, H.; Hughes, S. M.; Merkle, M. G.; Dahmen, U.; Wang, L.-W.; Alivisatos, A. P. Selective Facet Reactivity during Cation Exchange in Cadmium Sulfide Nanorods. *J. Am. Chem. Soc.* **2009**, *131*, 5285–5293.